# Effect of Particle Shape on Capillary Forces Acting on Particles at the Air−Water Interface

Nirmalya Chatterjee* and Markus Flury

Department of Crop and Soil Sciences, Washington State University, Puyallup, Washington 98371, United States

S *Supporting Information*

ABSTRACT: The capillary forces exerted by moving air−water interfaces can dislodge particles from stationary surfaces. The magnitude of the capillary forces depends on particle shape, orientation, and surface properties, such as contact angle and roughness. The objective was to quantify, both experimentally and theoretically, capillary force variations as an air−water interface moves over the particles. We measured capillary forces as a function of position, i.e., force−position curves, on particles of different shape by using force tensiometry. The particles (5 mm nominal size) were made of polyacrylate and were fabricated using a 3D printer. Experimental measurements were compared with theoretical calculations. We found that force−position curves could be classified into in three categories according to particle shapes: (1) curves for particles with round cross sections, such as spheroidal particles, (2) curves for particles with fixed cross sections, such as cylindrical or cubical particles, and (3) curves for particles with tapering cross sections, such as prismatic or tetrahedral particles. Spheroidal particles showed a continuously varying capillary force. Cylindrical or cubical particles showed pronounced pinning of the air−water interface line at edges. The pinning led to an increased capillary force, which was relaxed when the interface snapped off from the edges. Particles with tapering cross section did not show pinning and showed reduced capillary forces as the air−water interface line perimeter and displacement cross section continuously decrease when the air−water interface moved over the particles.
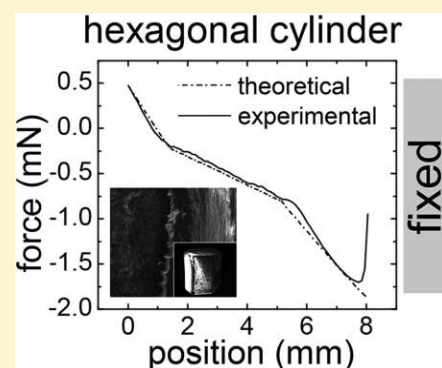
1. INTRODUCTION

Air−water interfaces play an important role in many physical phenomena occurring in nature.[1] A prominent example is the capillary force, which acts when a solid comes into contact with an air−water interface. The capillary force gives rise to capillary rise of water in a porous medium and to attachment of particles at the air−water interface. The strong attachment of particles to the air−water interface provides mechanisms for cleaning of wafers in microelectronics[2−5] as well as for immobilization[6,7] and mobilization of particles in porous media.[8−11]

Particles in contact with an air−water interface experience a force due to the surface tension and the pressure caused by the curvature of the air−water interface. The capillary force is the sum of the surface tension and pressure forces. The capillary force can exceed other interparticle forces, such as DLVO forces,[12−15] thereby leading to detachment and mobilization of particles from stationary surfaces.[2−4,9,16−18]

The capillary force acting on macroscopic particles has been quantified experimentally with force tensiometry.[9,19−21] Capillary forces acting on microscopic particles, mostly spheres, have been measured by using atomic force microscopy.[13,22−25] While most of these measurements have been conducted on spherical or spheroidal particles,[26,27] more recently, measurements with irregularly shaped particles and natural mineral particles have been reported.[9,21]

These measurements with irregularly shaped particles have shown that the shape and surface roughness play an important role in the interaction of the air−water interface with the particle. Natural particles often have sharp corners and edges from mechanical weathering and chipping, smooth, rounded faces from tumbling and from air and water erosion, and rough eroded surfaces due to chemical weathering—all on the same particle. Also, the characteristics of the mineral type lend to particular particle shapes, e.g., clay mineral particles tend to have flat plate-like shapes, while basaltic and granitic minerals have more granular, non-plate-like shapes. The presence of multiple such surface morphologies and features causes irregular particles to experience capillary forces which are a combination of features of multiple types of particle shapes. Particles with edges contribute to pinning of moving air−water interfaces at the edges, while corners oriented along the direction of the interface movement can cause progressive lowering of the capillary force as cross sections of the particles reduce gradually. The capillary force−position curves for irregular particles thus show a combination of features like abrupt force changes associated with interface pinning and snap-off and rounded and gradually reducing sections and random force variations from local roughness features.

The capillary force can theoretically be calculated with the Young−Laplace equation. Only in special cases the Young−

Laplace equation has an analytical solution. Numerical calculations of capillary forces have been reported for spherical particles.[19,20,27,28] Axisymmetric, but nonspherical, particle shapes have also been used for theoretical calculations,[21,29,30] but calculations become more complicated. No theoretical calculations have been reported for irregularly shaped particles.

Surface roughness affects the magnitude of the capillary force. The air−water interface can get pinned at macroscopic (e.g., corners, edges) and microscopic (e.g., surface irregularities) roughness. The pinning usually leads to an increase of the capillary force[1,21,31] and to a slip-pin behavior of a moving air−water interface. As most natural particles have rough surfaces, the slip-pin behavior of moving air−water interfaces is expected to be a common phenomenon.

In previous studies by our group, we have measured capillary forces using tensiometry on regularly and irregularly shaped particles.[15,21] Here, we expand on our previous studies by systematically investigating the effects of particle shapes on capillary forces. The objective of this study was to analyze, both theoretically and experimentally, the effect of particle shape on the capillary forces between the particles and the air−water interface. We experimentally measured the capillary force as a function of position, i.e., force−position curves, and we reconstructed the theoretical force−position curves based on numerical solutions of the Young−Laplace equation. We then compared the theoretical calculations with experimental measurements and deduced the specific topological features giving rise to the force−distance curve characteristics.

2. THEORY

2.1. Capillary Force. The theoretical basis of capillary force calculations involves numerically solving the Young−Laplace equation. Let us consider a particle in contact with a horizontal air−water interface, with the coordinate system comprising of the horizontal x,y-axes and the vertical z-axis. The theoretical capillary rise, z_c, against a surface of a solid particle can be calculated assuming that the air−water interface, at an extended distance ($x \rightarrow \infty$) from the axis of the particle, is undistorted and horizontal. For this case, the relationship between the capillary rise z_c, the horizontal distance of the contact line on the particle surface formed by the air−water interface from the z-axis, x_c, and the angle of inclination of the curved interface from the undisturbed interface, ϕ_c, is[15,19,21]

$$z_c = \frac{k_0(x_c)}{k_1(x_c)} \sin \phi_c \tag{1}$$

where the functions $k_0(x)$ and $k_1(x)$ are the modified Bessel functions of the second kind of orders 0 and 1, respectively.

The details of the calculation of capillary forces for axisymmetric particles are described in Zhang et al.[19] For nonspherical, axisymmetric particles, the capillary force vectors give rise to an undulating, multipolar force field. This multipolar force field has been observed experimentally[32−34] and characterized theoretically.[35−41]

In our previous work, we have measured and calculated capillary forces on natural sediment particles and model particles, and we calculated theoretical forces on the sediment particles assuming them to be triaxial ellipsoids.[21] We now extend our previous work to theoretically construct the force−position curves for a variety of particle shapes and compare them with experimental curves. In this work, we numerically solve for the capillary rise for each particle with the boundary

conditions dictated by their respective geometries. Following the approach described by Zhang et al.,[19] Shang et al.,[15] and Chatterjee et al.,[21] we calculate the force balance on a particle in contact with the air−water interface as

$$f = f_s + f_p + f_b = f_{cap} + f_b \tag{2}$$

where f is the net force on the particle, f_s, f_b, and f_p are surface tension, buoyancy, and pressure forces, respectively, and $f_{cap} = f_s + f_p$ is the capillary force. We assume the particle to be tared in the air phase, so the gravitational force can be omitted in eq 2.

When the particle is nonaxisymmetric or when surface inhomogeneities are present, the contact line itself is undulating.[32,33,35,36,40] However, these undulations do not increase the length of the contact line more than 10%;[21] thus, for mathematical simplicity, we do not correct for the increased length of the contact line. The three force components, f_s, f_b, and f_p, are calculated according to the geometry of the particle shape. The surface tension force, f_s, depends on the length of the contact line interacting with the air−water interface, the pressure force, f_p, depends on the area of the cross section at the plane of the contact line, and the buoyancy force, f_b, depends on the volume of the particle submerged under the air−water interface at the particular position.

2.2. Gibbs' Inequality. On an ideal particle with a smooth surface, the moving interface adjusts to an equilibrium position, with the contact angle at an equilibrium value for the particular three-phase interface. In a situation where a moving air−water interface interacts with a rough or edged particle, the roughness of the particle surface causes the interface to be attached at edges under nonequilibrium conditions. The nonequilibrium condition is manifested as a pinning of the air−water interface with a contact angle considerably different from the equilibrium contact angle. The range of values of the contact angle can be mathematically formulated by the Gibbs extension of the Young equation:[30]

$$\theta_0 < \theta < 180° - \alpha + \theta_0 \tag{3}$$

where θ_0 is the equilibrium contact angle for a smooth surface, θ is the nonequilibrium contact angle due to pinning of the air−water interface at the edge, and α is the wedge angle measured through the particles' solid phase. For example, for a cubical particle, the wedge angle is 90° at the cube's top or bottom edges. The edge causes the interface to get pinned and distorted, compared to a smooth surface without edges. As eq 3 shows, the pinning causes the actual contact angle to exceed the equilibrium contact angle. This increasing contact angle and the distortion of the air−water interface cause the capillary force to increase. When the contact angle passes a critical value, given by the Gibbs inequality, the air−water interface contact line snaps off from the edge and forms again at a new equilibrium position.

3. EXPERIMENTAL SECTION

3.1. Model Particles. The capillary force measurements were done on millimeter scale, UV-cured polyacrylate plastic particles made using a 3D printer. The density of the UV-cured polyacrylate plastic material was 1.09 g/cm³. We made nine particles of standard shape and categorized the particles according to their surface geometry and cross section of interaction with the air−water interface (Figure 1). First, we made a digital model of the particles by using the open source 3D modeling software Blender (Version 2.6.3) and saved it as a stereolithography (.stl) file. The model particles were attached to a
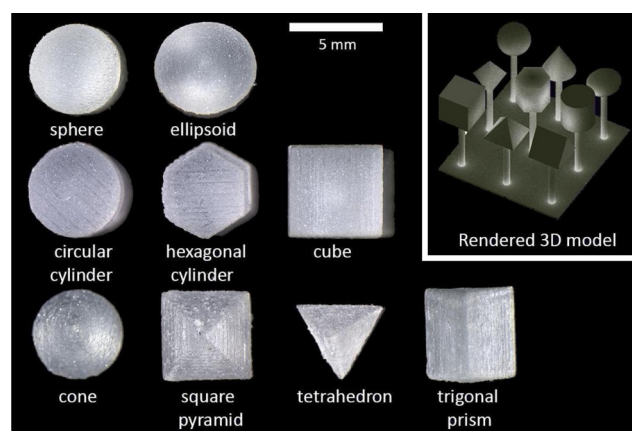
Figure 1. Dissection scope images of the nine model particles (view from the top). Inset: 3D rendering of the model used for 3D printing, including the attachment sticks and base plate.

0.5 mm thick common base plate using cylindrical stands (1 mm o.d. × 1 cm length) to facilitate single-piece fabrication during printing (Figure 1, inset). The .stl file was sent to Shapeways Inc. for 3D printing. Dimensions of the manufactured particles were measured using a digital caliper (Digit-Cal mm2000, Brown & Sharpe, Providence, RI) and are listed in Table 1.

Table 1. Characteristics of Model Particles

shape	schematic shape	top-view*	length (mm)	width (mm)	height (mm)
ROUNDED CROSS-SECTION					
sphere			4.95 (diameter)		
ellipsoid			5.56	4.89	2.57
FIXED CROSS-SECTION					
cylinder			5.02 (radius)		5.04
hexagonal cylinder			4.97	4.35	5.14
cube			5.20	5.04	5.04
TAPERED CROSS-SECTION					
cone			4.87 (radius)		5.04
square pyramid			4.92	4.82	3.67
tetrahedron			4.87	4.22	3.98
trigonal prism			5.00	4.90	4.28

*Arrows indicate how length and width were measured.

Based on the variation of the cross section interacting with the air–water interface, the particles can be classified into three main types (Figure 2): (a) particles with continuously varying cross section (sphere and ellipsoid), (b) particles with a fixed cross section (cylinder, hexagonal cylinder, and cube), and (c) particles with a linearly reducing or tapered cross section [cone, square pyramid, tetrahedron, and trigonal prism (tent-shaped)]. For further discussion of Figure 2 see section 4.

After printing, the individual particles were detached from the base plate and the attaching stands were cut off. The particles were then characterized for surface roughness and air–water contact angles. The

magnified views of the particles in Figure 3 show evidence of roughness due to the limited resolution of the 3D printer. The manufacture specified resolution of the printer was 100 μm (http://www.shapeways.com/materials/frosted-detail-design-guidelines). The air–water–particle surface contact angle on the particles was determined with a goniometer (CA Goniometer Model 50-00-115, Ramé-Hart Instrument Co., Netcong, NJ) using the method described in Chatterjee et al.[21] For the contact angle measurements, the particles were cleaned with ethanol and deionized water, dried, and then mounted on glass microscopy slides using double-sided adhesive tape. A microsyringe (steel needle with diameter of 0.5 mm) was used to put a 25 μL drop of water just next to the edge of the particle, so that the particle touched the side of the drop. The static contact angle of the particle material (UV-cured polyacrylate) was measured to be 136 ± 2°. The advancing and receding contact angles were measured on an expanding and a contracting drop of water, respectively, placed on the polyacrylate surface of the detached base plate. The advancing contact angle was 151 ± 2°, and the receding contact angle was 134 ± 4°.

3.2. Capillary Force Measurements. The particles were mounted on the lower end of J-shaped steel hooks using a small amount of polyacrylate glue (Dr. Bond Superglue, ITW Inc., Solon, OH). Prior to the measurement of the force–position curves, the mounted particles were cleaned with ethanol and deionized water and then dried in a jet of air. The details of recording the force–position curves on the tensiometer (Processor Tensiometer K100, Krüss GmbH, Hamburg, Germany) were described in detail previously.[21] Briefly, to determine the force–position curves, the upper end of the hook of a mounted particle was inserted into the tensiometer microbalance balance clip, and the microbalance was tared with the particle and hook in the air phase (Figure 4). An air–water interface was then moved over the stationary particle by incrementally raising a beaker of water at a speed of 6 mm/min. The forces exerted on the particle as a function of position of the air–water interface was recorded to generate a force–position curve until the air–water interface passed the top of the particle and the particle was fully immersed in water. For each particle, we recorded five replicate runs of the force–position curve and then averaged the data.

3.3. Surface Characterization with SEM. After the determination of the force–position curves, the particles were detached from the J-shaped hook and coated with platinum–palladium to a thickness of 3 nm under a sputter coater (Model 108auto, Cressington Scientific, Watford, England). We then examined the particles under a scanning electron microscope (SEM) equipped with a field emission electron gun (FEI Quanta 200F, FEI Co., Hillsboro, OR). The particles were kept oriented under the SEM in the same manner as for the force–position and contact angle measurements. If observed directly from the top, we obtain the xy-plane view of the particles. The SEM analysis of uncoated particles was not possible due to the nonconducting nature of polyacrylate plastic.

The SEM images of the particles and the magnified views of the surfaces depicting the roughness features and edges of the particles are shown in Figure 3. An estimate from the magnified views indicate that roughness feature dimensions were of the order of tens of micrometers. The magnified micrographs also indicate that the roughness on flat surfaces was generally less than on curved surfaces. The roughness contributes to both the deviation of the experimental force–position plots from theoretically calculated curves as well as the deviation of the actual contact angles from the macroscopically measured contact angles.

3.4. High-Speed Video Capture of Interface Pinning on Model Particles. To visualize the position and configuration of the air–water interface at the particles during the process of immersion, we used a high-speed video camera (MotionBLITZ Cube 3, Mikrotron GmbH, Unterschleissheim, Germany) equipped with a 50 mm, f/1.4 lens (Nikon Inc., Melville, NY). We shot 320 × 160 pixel videos at 1000 frames/s, with the camera attached to a standard laptop computer over a gigabit ethernet link. The lighting for the video photography was provided by a 1000 W halogen flood lamp placed 15 cm away from the sample platform.
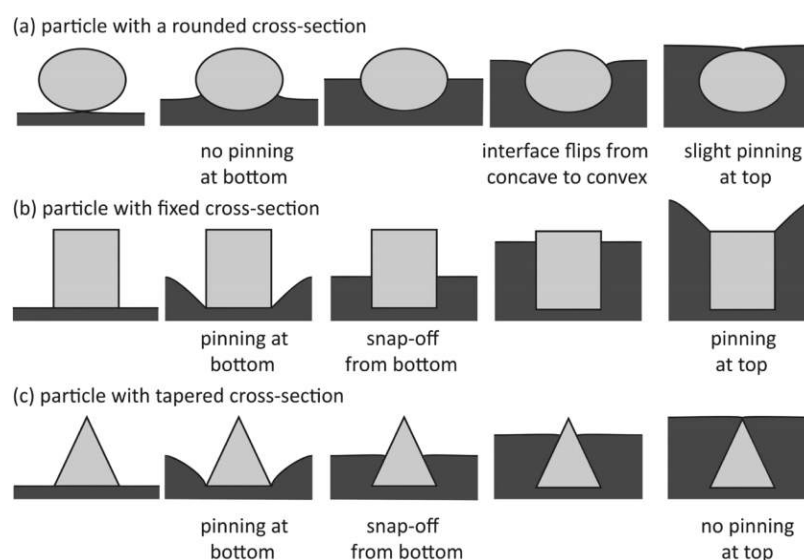
Figure 2. Schematic diagram of particle cross sections and air–water interface interaction for different positions of air–water interface on the particles. The air–water interface moves from bottom to top in the schematic diagrams (from left to right). The schematics depict an advancing contact angle of 90°.
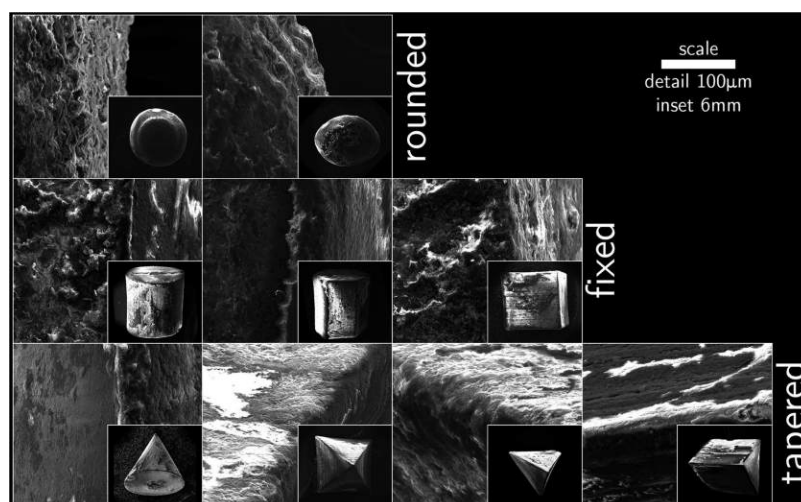

Figure 3. Scanning electron micrographs of the surface of the 3D printed particles. The detailed views are a 60× magnification of the particle overview images shown in the insets. The detailed views are taken on the edges of the particles to give an understanding of the size of roughness features.

3.5. Numerical Calculation of Capillary Forces. The capillary rise, z_c, was calculated as a function of position along the z-direction for each of the nine model particles according to eq 1. As the air–water interface is advancing during the immersion of the particles, we used the advancing contact angle (151°) for the numerical calculations. The calculated capillary rise was then used to determine the capillary force (sum of surface tension and pressure forces) experienced by the particle at that position. The total calculated force (capillary and buoyancy forces) was then plotted against the air–water interface position to obtain a theoretical force–position curve.

For the particles with a fixed cross section (cylinder, hexagonal cylinder, cube), which had an abrupt edge at the top, the air–water interface gets pinned at the edge. We calculated the capillary forces under conditions of pinning using the Gibbs' inequality (eq 3). The wedge angle for all three fixed cross-section particles was 90°. The pinning distance, z_{pin}, was obtained as the difference between the experimental distance over which the particle and the air–water interface were found to interact and the experimentally measured z-axis height of the particle (Table 2). We then calculated the force–position curve for angular increments over the total pinning distance.

4. RESULTS AND DISCUSSION

4.1. Results Expected from Theory. When a force–position curve is determined with the process tensiometer, the tensiometer microbalance measures the total force on the particle, i.e., the sum of the surface tension force, the pressure force, and the buoyancy force. Only the vertical component of the net force is registered, and we define downward forces as positive and upward forces as negative. The three categories of model particles are expected to interact differently with the air–water interface. Different stages of the position of the air–water interface on the particles are illustrated in Figure 2. In the following paragraphs, we discuss the shapes of the force–position curves that are expected from theory.

Particles with Rounded Cross Section. The particles with rounded cross sections are expected to have a smooth and continuously varying capillary force as a function of distance. The vertical component of the capillary force, while varying continuously, will change direction from a downward to an
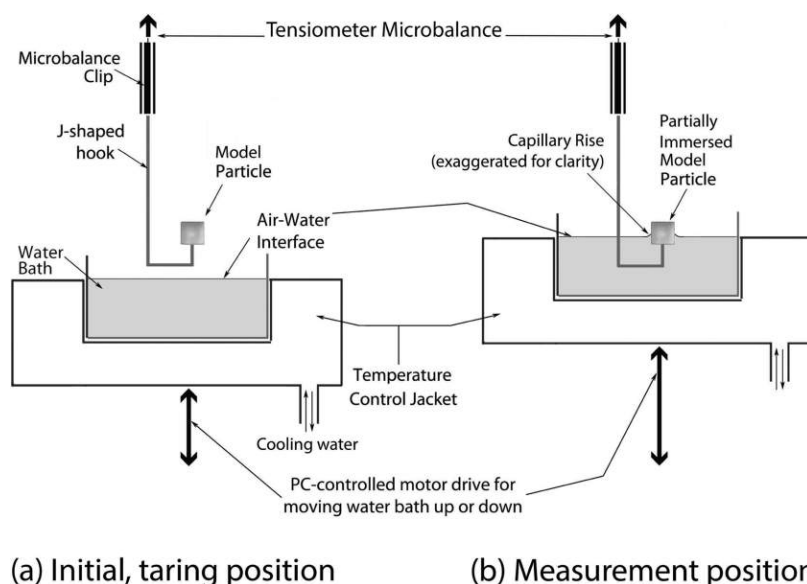
(a) Initial, taring position (b) Measurement position

Figure 4. Schematic of experimental setup for force−position curve measurements using a tensiometer. (a) Initial, taring position with particle and hook in air. (b) Measurement position with particle and hook, both partially immersed in water, and interacting with the air−water interface.

Table 2. Pinning Distances and Maximum Capillary Forces (Experimental and Theoretical)^a

| | dimensions | | | capillary force (μN) | | |
| | (mm) | | | experimental | | theoretical |
shape	$z_{max}^{\ b}$	$z_{pin}^{\ c}$	z_{pin}/z_{max}	f_{max}	$\Delta f_{snap\text{-}off}^{\ d}$	f_{max}
sphere	4.95	1.50	0.30	−1150	289	−672
ellipsoid	2.57	1.52	0.59	−1055	480	−1008
cylinder	5.04	2.00	0.40	−1751	689	−1927
hexagonal cylinder	5.14	2.81	0.55	−1701	607	−1780
cube	5.04	3.64	0.72	−2466	820	−2959
cone	5.04	0.58	0.11	−594	16	−679
square pyramid	3.67	1.44	0.39	−967	30	−680
tetrahedron	3.98	0.63	0.16	−437	3	−504
trigonal prism	4.28	1.83	0.43	−956	268	−841

^{a}Negative forces indicate upward forces, that is, forces pointing in direction from the water to the air phase. $^b z_{max}$ = height of particle along z-axis measured using a pair of calipers. $^c z_{pin}$ = total pinning distance along z-axis, measured from experimental force−position curves. $^d \Delta f_{snap\text{-}off}$ = force change due to the snapping off of the air−water interface leading to full immersion of the particle in water.

upward force due to the change of the interface curvature from concave to convex, caused by the fixed contact angle on the particle surface (Figure 2a).

At the initial contact, when the particle first touches the air−water interface, a positive, downward force is registered, due to a surface tension force and a pressure force. As the interface moves upward, the downward capillary force increases but soon reaches a maximum, after which the vertical component of the capillary force decreases more and more because the surface tension component of the capillary force starts pointing in horizontal direction. For a particle with 90° contact angle, the vertical component of the capillary force is zero exactly when the air−water interface is at the equatorial plane. As the air−water interface contact line passes the equatorial plane, the capillary force changes direction. For our experimental particles (contact angle θ = 151°), this change in direction of the vertical

component of the capillary force is expected to occur at around 29° latitude below the equator. As the air−water interface contact line continues to move upward, the particle begins to experience an upward pointing (negative) capillary force. Because of symmetry, the now upward pointing capillary force passes through a negative maximum value, before the force reduces again because of the reduction in the length of the contact line (perimeter).

The force−position curve shows the net vertical force on the particle as a function of position of the air−water interface. The position is measured as the distance of the air−water interface from the bottom boundary of the particle. The contact line would ultimately reduce to a very small perimeter at the top of the particle (Figure 2a), causing the surface tension force and the distortion of the air−water interface due to the contact line to be small, which cause the pressure force to be proportionally small. At that point, the largest force registered by the tensiometer is the negative and upward pointing buoyancy force. For a smooth, round particle we do not expect any pinning to occur. This behavior of the force will give rise to a sinusoidal force−position curve as schematically depicted in Figure 5.
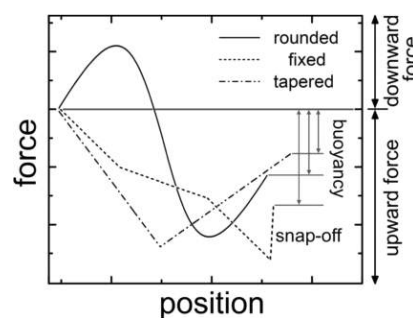

Figure 5. Schematic of force−position curves during immersion for model particles with different categories of cross sections. The vertical double arrows inside the figure indicate the buoyancy force for the completely immersed particles. Force and position axes have arbitrary units.

Particles with Fixed Cross Section. The particles with fixed cross sections are expected to have a constant value of both the surface tension and the pressure forces (total capillary force), irrespective of the position of the air−water interface line, because the shape of the air−water interface remains identical as the interface moves along the fixed cross section (Figure 2b). The buoyancy force is expected to increase progressively. The combined value of the force registered on the tensiometer should, thus, be progressively increasing (upward pointing) with the increase being due to buoyancy force only (Figure 5).

At the edges of the fixed cross-section particles, we can expect interfacial pinning (Figure 2b). Following the Gibbs' inequality, the contact angle will increase at the edges until the interface slips off. At the bottom of the particle the interface will slip off onto the vertical side of the particle; at the top of the particle the interface will snap-off from the particle, thus immersing the whole particle into the water. So, we expect the pinning phenomena to be similar at both the bottom and the top edges; the slopes of the force−position curve should be similar for both edges but different from when the interface is sliding along the vertical face of the particle. Thus, we expect a three segment form of the force−position curve for the particles of fixed cross section (Figure 5). In the first segment, we have a constantly increasing, negative, upward force as long as the interface is pinned to the bottom. This is followed by a segment with an increasing, negative upward force, due to the fixed contact line and increasing buoyancy force. Finally, when the air−water interface reaches the top edge of the particle, it gets pinned, and the negative upward force increases again, similar to the case with the bottom pinning. The final expected feature is the snap-off of the interface from the top edge of the particle.

Particles with Tapered Cross Section. The particles with tapered cross sections are expected to have a constantly decreasing value of both the surface tension and the pressure forces because the cross-sectional area and the length of the contact line are continuously decreasing as we proceed from the broad bottom of the particles to their pointed top (Figure 2c). The buoyancy force is expected to progressively increase as the particle is immersed in the water; however, the rate of increase of the buoyancy force should slow down as the particle tapers off at the top. The overall shape of the force−position curve should have two segments (Figure 5). The first segment is an increasing, upward pointing, negative force due to an increasing surface tension force and a pressure force as long as the air−water interface remains pinned to the bottom edge. The second segment, when the interface moves along the side walls of the particle, is also negative and upward pointing, but the negative force becomes continuously smaller (i.e., the force−position curve shows a positive slope) as the cross section of the particle decreases. The plot ends at the negative value of the buoyancy force of the totally immersed particle. No pinning is expected at the top because the tapered particles have a pointed end; i.e., ending in a point for the cone, square pyramid, and the tetrahedron or a line for the trigonal prism (tent-shaped).

4.2. Observations from High-Speed Videos. The videos played in slow motion provide interesting insights into the interaction of the air−water interface with the particles, illustrating the locations of pinning due to sharp edges as well as roughnesses originating from the printing process (see Supporting Information). The videos show the depression of the air−water interface due to the pinning effect and the

curvature of the interface at various positions along the surface of the particle. Details are discussed in the Supporting Information.

4.3. Description of Experimentally Obtained Force− Position Curves. Figure 6 shows a typical experimental force−
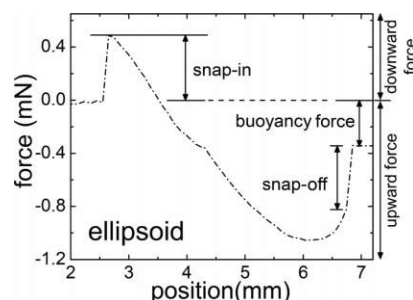

Figure 6. A typical experimental force−position curve, measured with a processor tensiometer, obtained for an ellipsoidal particle. Note the presence of a snap-off even though a snap-off is not expected for a particle of rounded cross section. The advancing contact angle for the particle is $\theta = 151 \pm 2°$.

position curve measured on the process tensiometer for an ellipsoidal particle. There is a pronounced downward (i.e., positive) force at the onset indicated by a spike in the plot. This feature is due to the snap-in of the air−water interface at the juncture of the steel hook and the bottom of the model particles (Figure 4). This is an experimental artifact due to the presence of the steel hook, which alters the initial shape of the force−position curve and the starting point of the subsequent force−position curve due to the particle interacting with the air−water interface. However, the remainder of the points on the plot are not affected by this artifact and follow the expected curve from a freely suspended particle (without the hook). Figure 6 also shows a constant force at the end of the curve, which indicates that the particle is totally immersed in water. The constant force registered at the end is the buoyancy force, which manifests as a negative, upward pointing force.

For all the following experimental force−position curves, to make the comparisons independent of the variations due to the mounting of the hook, we removed the spike at the onset and set this position as the zero position. We also removed the part at the end where only the buoyancy force is being measured. We only compare the curves during the immersion of the particles.

4.4. Reconstruction and Interpretation of Force− Position Curves. Figure 7 shows the experimentally obtained and theoretically calculated force−position curves for all nine particles. Table 2 lists the maximum deflection of the air−water interface due to pinning as well as the maximum experimental and theoretical forces experienced by the particles as determined from the force−position curves. In the following, we discuss the data for each category of particles.

Particles with Round Cross Sections. The experimental force−position curves of the spheroidal particles (sphere and ellipsoid) have a smooth, rounded shape, as is expected from theory (Figure 7a,b). The experimental curves differ in two key aspects from the theoretically calculated curves. First, the round shape of the curve at the onset are obscured by the snap-in phenomena and artifacts due to the presence of the hook. Second, the experimental curves extends over a longer distance than the actual z-axis dimension of the particle. This extension
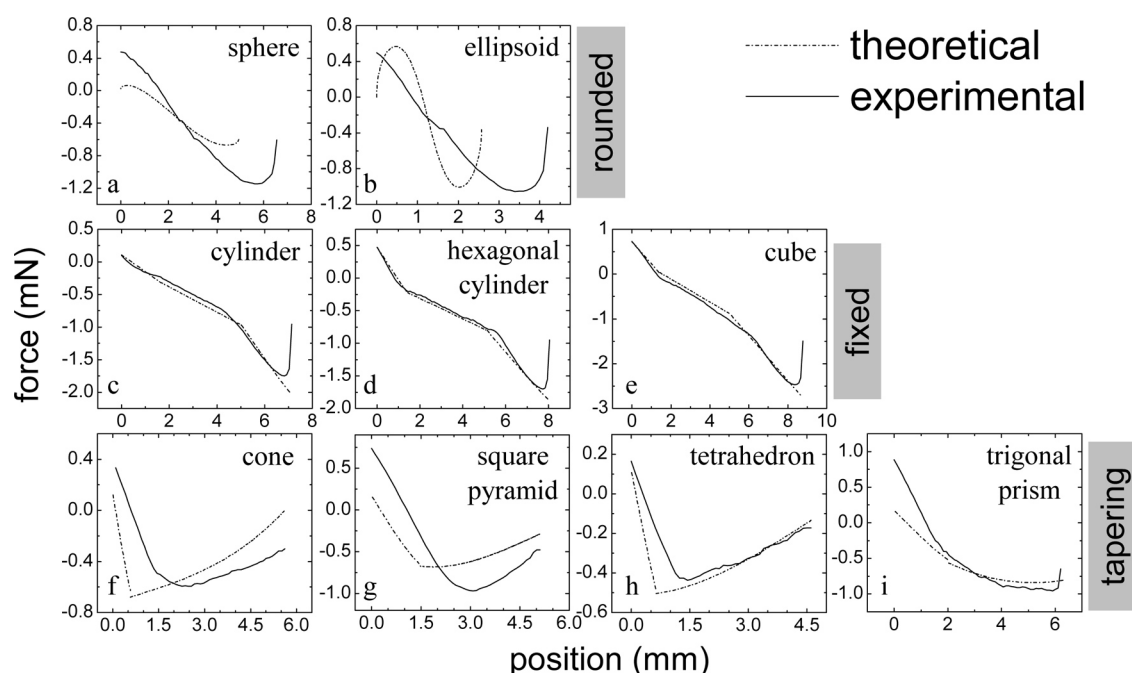
Figure 7. Comparison of experimental and theoretically reconstructed force–position curves during immersion for nine model particles. The advancing contact angle for the particles is $\theta = 151 \pm 2°$.

is due to (1) snap-in of the interface at the bottom and associated pinning due to attachment of the hook, (2) local pinning of the interface on roughness features on the particle surface, and (3) the pinning of the interface at the top of the particle, again due to surface roughness. Further support of these explanations is provided when we scale the theoretical curves over the same distance as the experimental curves. The scaled theoretical curves, especially for the ellipsoid, match the experimental curves well (Figure S2, Supporting Information). For the spherical particle, the shape of the curve is similar, but the magnitudes of the forces calculated using theory are lower than those observed experimentally.

The difference between the total distance of interaction of the particle with the air–water interface and its actual height is denoted by its pinning distance, z_{pin} (Table 2). The distance z_{pin} is the cumulative deflection of the air–water interface from its flat, undisturbed surface. The theoretically calculated forces at corresponding positions are in best agreement with experimental values for the ellipsoid, as reported previously in Chatterjee et al.;[21] however, the flatter shape of the ellipsoid also causes a more pronounced pinning than compared to the spherical particle, as can be seen by the increased ratio of z_{pin}/z_{max}. The magnitudes of the forces calculated theoretically are, in general, smaller than the experimental forces due to the absence of local pinning considered in the calculations.

Particles with Fixed Cross Sections. The experimental force–position curves for the particles with a fixed cross-sectional area (Figure 7c–e) show the expected three segment form. The distinct slope changes between the segments in the theoretical curves are, however, less pronounced in the experimentally observed force–position curves. This is because the particles did not have perfectly sharp edges, and the interface crept around the edges of the particles. This creeping of the interface around the sharp edges could be observed in the high-speed videos (see Supporting Information). The creeping phenomena around the edge caused the slope of the experimental force–position curve to change more gradually

than that in the theoretical curve. Because of the creeping of the interface over the top edge, the snap-off from the top actually occurs from the top face rather than from the top edge, thus causing the experimental maximum force to be less than the theoretical maximum force (Figure 7c–e).

Particles with Tapered Cross Section. The experimental force–position curves for the particles with a tapered cross section (Figure 7f–i) show a shape which reflects the progressively decreasing cross section of the particle interacting with the air–water interface, as the interface line moves toward the top of the particle. The eventual vanishing of the capillary force is apparent in the cone, the square pyramid, and the tetrahedron, all of which show a lack of interface pinning at the top. The square tent which has a straight top edge shows a small pinning (Figure 7i). The general trend in the force–position curves can be explained by the progressive decrease in both the surface tension force, due to decreasing length of the contact line, and the pressure force, due to decreasing area of the cross section. The rate of increase of the buoyancy force also slows down as the particle tapers toward the top; therefore, the total upward force gradually reduces to the final baseline value of the buoyancy force. The theoretical reconstructions of the force–position curves follow a similar trend as the experimental curves. The quantitation of the force magnitude is, however, not exact due to the local pinning and change in contact angles as discussed above (Table 2).

4.5. Maximum Capillary Forces and Snap-Off Forces. Except for the cone, square pyramid, and tetrahedron (Figure 7f–h), the experimental force–position curves for all other particles show a pinning effect and snap-off of the air–water interface at the top. This snap-off of the interface is manifested as a sharp rise in the force–position curve and is due to the sudden loss of the surface tension and pressure force components.

A comparison of the force–position curves of the three classes of particles shows that the snap-off is the most abrupt for the particles with fixed cross section, followed by that in the

rounded particles. The particles of tapered cross section show an almost complete lack of pinning at the top edge. The particles have different snap-off forces and maximum capillary forces on account of their shape.

Table 2 lists the maximum, upward (negative) forces experienced by each model particle as well as the snap-off forces. The data show that fixed cross-section and sharp-edged particles experience the largest forces. Particles with tapered cross sections, however, show smaller maximum capillary forces than even the rounded cross-section particles, a result of their smaller contact lines and cross sections.

The theoretical maximum force is best estimated for the ellipsoid. The theoretical estimate of the maximum force for the sphere is lower than the experimental value, likely because we did not take into consideration the local pinning of the interface. For all other particles, except the trigonal prism, the theoretically estimated maximum force is larger than the experimentally measured maximum force. This is because for the experimental curves, the air−water interface crept around the edges of the particles, and thus, the magnitude of the forces due to interface pinning was reduced. However, for all the particles, the interaction distance along the z-axis is longer for the experimental curves ($z_{pin}/z_{max} > 0$), which reinforces the importance of localized pinning effects due to roughness of the surfaces on the capillary forces (Table 2).

5. IMPLICATIONS

Capillary forces acting on particles at the air−water interface have been found to exceed DLVO and gravity forces,[9,12,13,15] and the smaller the particles, the more dominant the capillary forces become. Moving air−water interfaces have been implicated in the detachment of colloidal particles from solid surfaces at the pore scale[2,3,10,16] as well as at the porous medium scale.[8,10,11,42,43] Thus, capillary forces play an important role in colloid mobilization from matrices, like soils and sediments. Situations of moving air−water interfaces in soils arise during water drainage and infiltration events.

The force−position curves for particles interacting with moving air−water interfaces show a variety of features, dictated by the particle shape, surface roughness, and particle orientation. Pertinent features are the pinning and creeping of air−water interfaces over sharp edges as well as the pinning of interfaces at surface roughnesses and the associated increase of contact angles. The characteristics of the force−position curves allows us to deduce the magnitude and dynamics of the capillary forces acting on a particle. Our studies indicate that force−position curves can be broadly classified into three different categories based on shape (in direction of the air−water interface movement): (1) round particles, (2) fixed cross-section particles, and (3) tapered particles. Among these particle shapes, tapered particles are least likely to be dislodged by a moving air−water interface, whereas particles with edges or particles with surface roughness get most readily mobilized.

■ ASSOCIATED CONTENT

Ⓢ Supporting Information

High-speed movies depicting the interaction of the moving air−water interface with the model particles for each model particle; a figure showing a comparison of experimental force−position curves and theoretical force−position curves scaled over the experimental interaction distance for a spherical and an ellipsoidal particle. This material is available free of charge via the Internet at http://pubs.acs.org.

■ AUTHOR INFORMATION

Corresponding Author
*Phone 1-509-432-9533, e-mail c_nirmalya@wsu.edu (N.C.).

Notes
The authors declare no competing financial interest.

■ REFERENCES

(1) de Gennes, P.-G.; Brochard-Wyart, F.; Quéreé, D. *Capillarity and Wetting Phenomena. Drops, Bubbles, Pearls, Waves*; Springer: New York, 2004.
(2) Leenaars, A. F. M.; O'Brien, S. B. G. Particle removal from silicon substrates using surface tension forces. *Philips J. Res.* **1989**, *44*, 183−209.
(3) Noordmans, J.; Wit, P. J.; van der Mei, H. C.; Busscher, H. J. Detachment of polystyrene particles from collector surfaces by surface tension forces induced by air-bubble passage through a parallel plate flow chamber. *J. Adhes. Sci. Technol.* **1997**, *11*, 957−969.
(4) Gomez-Suarez, C.; Noordmans, J.; van der Mei, H. C.; Busscher, H. J. Removal of colloidal particles from quartz collector surfaces as simulated by the passage of liquid-air interfaces. *Langmuir* **1999**, *15*, 5123−5127.
(5) Gomez-Suarez, C.; Noordmans, J.; van der Mei, H. C.; Busscher, H. J. Detachment of colloidal particles from collector surfaces with different electrostatic charge and hydrophobicity by attachment to air bubbles in a parallel plate flow chamber. *Phys. Chem. Chem. Phys.* **1999**, *1*, 4423−4427.
(6) Wan, J. M.; Tokunaga, T. K. Film straining of colloids in unsaturated porous media: conceptual model and experimental testing. *Environ. Sci. Technol.* **1997**, *31*, 2413−2420.
(7) Veerapaneni, S.; Wan, J.; Tokunaga, T. Motion of particles in film flow. *Environ. Sci. Technol.* **2000**, *34*, 2465−2471.
(8) Zhuang, J.; McCarthy, J. F.; Tyner, J. S.; Perfect, E.; Flury, M. In-situ colloid mobilization in Hanford sediments under unsaturated transient flow conditions: Effect of irrigation pattern. *Environ. Sci. Technol.* **2007**, *41*, 3199−3204.
(9) Shang, J.; Flury, M.; Chen, G.; Zhuang, J. Impact of flow rate, water content, and capillary forces on *in situ* colloid mobilization during infiltration in unsaturated sediments. *Water Resour. Res.* **2008**, *44*, W06411 DOI: 10.1029/2007WR006516.
(10) Sharma, P.; Abdou, H.; Flury, M. Effect of the lower boundary condition and flotation on colloid mobilization in unsaturated sandy sediments. *Vadose Zone J.* **2008**, *7*, 930−940.
(11) Cheng, T.; Saiers, J. E. Mobilization and transport of in situ colloids during drainage and imbibition of partially saturated sediments. *Water Resour. Res.* **2009**, *45*, W08414 DOI: 10.1029/2008WR007494.
(12) Scheludko, A.; Toshev, B. V.; Bojadjiev, D. T. Attachment of particles to a liquid surface (capillary theory of flotation). *J. Chem. Soc., Faraday Trans. 1* **1976**, *72*, 2815−2828.
(13) Preuss, M.; Butt, H. Direct measurement of particle-bubble interactions in aqueous electrolyte: dependence on surfactant. *Langmuir* **1998**, *14*, 3164−3174.

(14) Sharma, P.; Flury, M.; Zhou, J. Detachment of colloids from a solid surface by a moving air-water interface. *J. Colloid Interface Sci.* **2008**, *326*, 143−150.

(15) Shang, J.; Flury, M.; Deng, Y. Force measurements between particles and the air-water interface: Implications for particle mobilization in unsaturated porous media. *Water Resour. Res.* **2009**, *45*, W06420 DOI: 10.1029/2008WR007384.

(16) Aramrak, S.; Flury, M.; Harsh, J. B. Detachment of deposited colloids by advancing and receding air-water interfaces. *Langmuir* **2011**, *27*, 9985−9993.

(17) Lazouskaya, V.; Wang, L.-P.; Gao, H.; Shi, X.; Czymmek, K.; Jin, Y. Pore-scale investigation of colloid retention and mobilization in the presence of a moving air-water interface. *Vadose Zone J.* **2011**, *10*, 1250−1260.

(18) Aramrak, S.; Flury, M.; Harsh, J. B.; Zollars, R. L.; Davis, H. P. Does colloid shape affect detachment of colloids by a moving air-water interface? *Langmuir* **2013**, *29*, 5770−5780.

(19) Zhang, L.; Ren, L.; Hartland, S. More convenient and suitable methods for sphere tensiometry. *J. Colloid Interface Sci.* **1996**, *180*, 493−503.

(20) Zhang, L.; Ren, L.; Hartland, S. Detailed analysis of determination of contact angle using sphere tensiometry. *J. Colloid Interface Sci.* **1997**, *192*, 306−318.

(21) Chatterjee, N.; Lapin, S.; Flury, M. Capillary forces between sediment particles and an air-water interface. *Environ. Sci. Technol.* **2012**, *46*, 4411−4418.

(22) Preuss, M.; Butt, H. J. Measuring the contact angle of individual colloidal particles. *J. Colloid Interface Sci.* **1998**, *208*, 468−477.

(23) Gillies, G.; Kappl, M.; Butt, H. Direct measurements of particle-bubble interactions. *Adv. Colloid Interface Sci.* **2005**, *114*, 165−172.

(24) Englert, A.; Krasowska, M.; Fornasiero, D.; Ralston, J.; Rubio, J. Interaction force between an air bubble and a hydrophilic spherical particle in water, measured by the colloid probe technique. *Int. J. Miner. Process.* **2009**, *92*, 121−127.

(25) Yamamoto, T.; Harada, Y.; Fukui, K.; Yoshida, H. AFM investigation of the surface properties of silica particles dispersed by bead milling. *Colloids Surf., A* **2010**, *362*, 97−101.

(26) Gunde, R.; Hartland, S.; Mader, R. Sphere tensiometry: a new approach to simultaneous and independent determination of surface tension and contact angle. *J. Colloid Interface Sci.* **1995**, *176*, 17−30.

(27) Ecke, S.; Preuss, M.; Butt, H. J. Microsphere tensiometry to measure advancing and receding contact angles on individual particles. *J. Adhes. Sci. Technol.* **1999**, *13*, 1181−1191.

(28) Princen, H. M. Equilibrium shape of interfaces, drops, and bubbles. Rigid and deformable particles at interfaces. *Surf. Colloid Sci.* **1969**, *2*, 1−84.

(29) Hesla, T. I.; Joseph, D. D. The maximum contact angle at the rim of a heavy floating disk. *J. Colloid Interface Sci.* **2004**, *279*, 186−191.

(30) Singh, P.; Joseph, D. D. Fluid dynamics of floating particles. *J. Fluid Mech.* **2005**, *530*, 31−80.

(31) Ally, J.; Kappl, M.; Butt, H.-J. Adhesion of particles with sharp edges to air-liquid interfaces. *Langmuir* **2012**, *28*, 11042−11047.

(32) Loudet, J. C.; Alsayed, A. M.; Zhang, J.; Yodh, A. G. Capillary interactions between anisotropic colloidal particles. *Phys. Rev. Lett.* **2005**, *94*, 018301.

(33) Loudet, J. C.; Yodh, A. G.; Pouligny, B. Wetting and contact lines of micrometer-sized ellipsoids. *Phys. Rev. Lett.* **2006**, *97*, 018304.

(34) Lewandowski, E. P.; Bernate, J. A.; Searson, P. C.; Stebe, K. J. Rotation and alignment of anisotropic particles on nonplanar interfaces. *Langmuir* **2008**, *24*, 9302−9307.

(35) Stamou, D.; Duschl, C.; Johannsmann, D. Long-range attraction between colloidal spheres at the air-water interface: The consequence of an irregular meniscus. *Phys. Rev. E* **2000**, *62*, 5263−5272.

(36) Kralchevsky, P. A.; Denkov, N. D.; Danov, K. D. Particles with an undulated contact line at a fluid interface: interaction between capillary quadrupoles and rheology of particulate monolayers. *Langmuir* **2001**, *17*, 7694−7705.

(37) Danov, K. D.; Kralchevsky, P. A.; Naydenov, B. N.; Brenn, G. Interactions between particles with an undulated contact line at a fluid interface: Capillary multipoles of arbitrary order. *J. Colloid Interface Sci.* **2005**, *287*, 121−134.

(38) van Nierop, E. A.; Stijnman, M. A.; Hilgenfeldt, S. Shape-induced capillary interactions of colloidal particles. *Europhys. Lett.* **2005**, *72*, 671−677.

(39) Lehle, H.; Oettel, M. Importance of boundary conditions for fluctuation-induced forces between colloids at interfaces. *Phys. Rev. E* **2007**, *75*, 011602.

(40) Lehle, H.; Noruzifar, E.; Oettel, M. Ellipsoidal particles at fluid interfaces. *Eur. Phys. J. E: Soft Matter Biol. Phys.* **2008**, *26*, 151−160.

(41) Danov, K. D.; Kralchevsky, P. A. Capillary forces between particles at a liquid interface: General theoretical approach and interactions between capillary multipoles. *Adv. Colloid Interface Sci.* **2010**, *154*, 91−103.

(42) Saiers, J. E.; Lenhart, J. J. Colloid mobilization and transport within unsaturated porous media under transient-flow conditions. *Water Resour. Res.* **2003**, *39*, 1019 DOI: 10.1029/2002WR001370.

(43) Saiers, J. E.; Hornberger, G. M.; Garower, D. B.; Herman, J. S. The role of moving air-water interfaces in colloid mobilization within the vadose zone. *Geophys. Res. Lett.* **2003**, *30*, 2083 DOI: 10.1029/2003GL018418.